Synergistic Design of Practical High-Capacity Satellite Communication: Leveraging FFT-Based Digital Beamforming

JUAN ANDRÉS VÁSQUEZ-PERALVO[1], *MEMBER, IEEE*, VU NGUYEN HA[1], *SENIOR MEMBER, IEEE* LUIS MANUEL GARCÉS-SOCARRÁS[1], *MEMBER, IEEE*, TI TI NGUYEN[1], *MEMBER, IEEE*, RAUDEL CUIMAN[1], *MEMBER, IEEE*, JORGE LUIS GONZÁLEZ-RIOS[1], *MEMBER, IEEE*, JUAN CARLOS MERLANO DUNCAN[1], *SENIOR MEMBER, IEEE* SYMEON CHATZINOTAS[1], *FELLOW MEMBER, IEEE*

[1]Interdisciplinary Centre for Security, Reliability, and Trust (SnT), Luxembourg, L-1855 Luxembourg (e-mail: juan.vasquez@uni.lu, vu.nguyen@uni.lu, luis.garces@uni.lu, titi.nguyen@uni.lu raudel.cuiman@uni.lu, jorge.gonzalez@uni.lu juan.duncan@uni.lu, Symeon.Chatzinotas@uni.lu)

Corresponding author: Juan Andrés Vásquez Peralvo (e-mail: juan.vasquez@uni.lu).

This work was supported by European Space Agency under the project number 4000134678/21/UK/AL "EFFICIENT DIGITAL BEAMFORMING TECHNIQUES FOR ON-BOARD DIGITAL PROCESSORS (EGERTON)" (Opinions, interpretations, recommendations and conclusions presented in this paper are those of the authors and are not necessarily endorsed by the European Space Agency). This work was supported by the Luxembourg National Research Fund (FNR), through the CORE Project (C^3): Cosmic Communication Construction under Grant C23/IS/18116142/C3.

ABSTRACT The growing demand for high-capacity satellite communications, particularly in Medium Earth Orbit (MEO) and Low Earth Orbit (LEO) constellations, has made digital beamforming essential to enhance system performance by producing simultaneous beams. Among various techniques, Fast Fourier Transform (FFT)-based beamforming is favored for its power efficiency and effectiveness in terms of Signal-to-Interference Ratio (SIR) when the number of antennas matches the number of beams. However, to reduce costs and complexity in the RF-chain, the number of antennas is often reduced relative to the number of beams, compromising beam orthogonality and degrading the SIR. This paper investigates the combination of techniques to mitigate this degradation, including regular spaced triangular-lattice beams and antennas, hexagonal subarray lattices, 4-color scheme, and tapering, all working synergistically to enhance the overall SIR. The proposed method employs regular hexagonal sampling grids, enabling the generation of triangular-lattice beams using standard rectangular FFT-routines. By avoiding interpolation, this approach minimizes artifacts in beam pattern generation over wide fields of view and preserves the SIR, making it particularly suitable for satellite applications. The simulation results demonstrate that the proposed strategy, using a 16-point FFT-beamforming approach with only 100 antenna elements, significantly enhances the SIR by nearly 20 dB compared to the regular scenario.

INDEX TERMS Satellite communications, digital beamforming, phased arrays

I. INTRODUCTION

THE Fast Fourier Transform (FFT) algorithm is widely recognized for its efficiency in digital beamforming, particularly due to its ability to transform spatial data into the frequency domain with significantly reduced computational complexity. Compared to other beamforming algorithms, such as Minimum Mean Square Error (MMSE) beamforming, which requires computationally-intensive matrix inversion [1], the FFT offers a more efficient alternative by relying on sums and multiplications. Table 1 presents a more detailed comparison of different beamforming algorithms against FFT-beamforming.

The computational efficiency of the FFT stems from its reduction of the Discrete Fourier Transform (DFT) complexity from $\mathcal{O}(N^2)$ to $\mathcal{O}(N \log N)$, where N represents the number of data points [2]. This reduction is achieved by recursively breaking down the DFT into smaller sub-problems, allowing the FFT to exploit symmetries and redundancies in the

TABLE 1: Comparison of Digital Beamforming Techniques.

Technique	Load	Multi-Beam	Adaptability
Delay-and-Sum	Very Low	Low	Low
FFT-Based (this work)	Low	High	Medium
Zero-Forcing (ZF)	Medium	High	Low
MVDR (Capon)	Medium	Medium	High
LCMV	High	High	High
Eigen-Based	High	Medium	Medium
Max. Likelihood	Very High	Low	Medium

DFT calculations. Consequently, the number of required multiplications and additions is greatly reduced, leading to reduced power consumption in processing units [3]. This makes the FFT particularly suitable for real-time applications such as beamforming in large antenna arrays, especially in scenarios where a high number of beams must be generated with low complexity and low power.

These characteristics have attracted significant attention from both academia and industry due to their advantages in complexity reduction, power efficiency, and hardware compactness. For instance, in terms of hardware efficiency, [4] demonstrates that a non-quantized approach consumes less power, while the quantized implementation eliminates the need for DSP blocks. Additionally, the European Space Agency (ESA) has published a patent [5] that advocates FFT-based beamforming with pre- and post-processing stages for low-power operation in dense, non-uniform beam scenarios. On the implementation side, Xilinx/AMD's FFT LogiCORE IP provides a highly configurable streaming FFT hardware platform, which has become widely adopted for spatial FFT beamforming in satellite communications and emerging 5G systems [6].

Despite these advantages, FFT-based beamforming presents several inherent limitations. It is traditionally constrained to regular antenna lattices, as the algorithm relies on orthogonality that maps beams to fixed, grid-aligned directions. Moreover, it requires that the number of antenna elements per dimension N matches the FFT size M (i.e., $N = M$) to maintain orthogonality and minimize inter-beam interference [7]. This orthogonality ensures that the nulls of one beam coincide with the main lobes of adjacent beams, significantly reducing mutual interference. However, this setup restricts beam reconfigurability and makes FFT beamforming less suitable for adaptive interference mitigation, or non-uniform antenna placements. In addition, FFT-based beamforming inherently generates fixed beam directions, and in wideband scenarios, it suffers from beam squint, which further limits its flexibility. Recent studies have addressed some of these limitations using techniques such as precoding [8], and FFT extensions to non-equispaced data by Non-Uniform FFT (NUFFT) [5], thus enabling more dynamic and irregular configurations. Nevertheless, a critical and understudied challenge arises when the number of antenna elements is lower than the FFT index (i.e., $N < M$), a common condition in systems constrained by hardware resources.

However, in many practical scenarios, particularly in satellite communications and size-constrained systems, it is desirable to reduce the number of antenna elements ($N < M$). In such cases, orthogonality is lost, because the nulls of one beam no longer align with the main lobes of neighboring beams, leading to increased interbeam interference and degraded SIR.

This limitation introduces several open research challenges for FFT-based beamforming, particularly in designing strategies that can mitigate inter-beam interference when antenna count is constrained. These challenges motivate the need for innovations in lattice configuration, subarray design, beam selection, and array excitation shaping.

The feasibility of FFT-based beamforming has been demonstrated in numerous studies. For example, early work by Mitsubishi in 1996 [9] implemented a 16-beam FFT beamformer using an Application-Specific Integrated Circuits (ASIC) for mobile satellite communication, leveraging a rectangular array with $N = M$ to ensure orthogonality. More recently, [10] extended this approach to a 32-point FFT, generating 1024 simultaneous beams in the 5.8 GHz band, again using $N = M$ rectangular arrays. Similarly, a 16-point multiplierless DFT approximation was proposed in [11] for linear arrays with the same dimensional match.

In contrast, on-board satellite implementations exploring the $N < M$ case are relatively scarce. One such example is [12], where the authors developed a 16-point 2D-FFT beamformer using quantized DFT and rectangular lattices. However, this work did not explore the impact of array lattice geometry or inter-beam interference mitigation. Lattice geometry has been explored in more theoretical contexts, such as the work of Angeletti [13], who used the multi-dimensional DFT (MD-DFT) to examine beam tessellations over Voronoi and parallelogram regions. Other foundational works, including [14], [15], have extended these ideas to triangular and nested lattice structures, though still under ideal conditions.

Recent studies have also considered techniques like inverse Fourier transform (IFT)-based tapering [16] to suppress sidelobes. However, these works mainly target rectangular apertures and do not directly address how to compensate for the loss of orthogonality in scenarios where $N < M$. Therefore, there is a clear gap in the literature regarding systematic methods for improving SIR in FFT-based systems when the $N < M$.

To address these challenges, this article proposes a coherent strategy to enhance SIR in FFT beamforming when the number of antenna elements is constrained. The novelty lies in the systematic integration of the following design components:

- **Triangular-lattice array geometry**, to reduce grating lobes and aliasing under wide-angle scanning.

- **Hexagonal subarray tiling**, to enable efficient grouping of antenna elements and reduce RF chain requirements.
- **Triangular-lattice beam placement**, to align FFT beams with array geometry for minimal distortion.
- **Beam deactivation strategies**, to suppress beam patterns with high interference or low utility.
- **Amplitude tapering**, to reduce Side Lobe Level (SLL) and compensate for non-orthogonality.

Rather than combining these techniques independently, we examine their synergistic behavior in constrained FFT beamforming systems. Notably, we demonstrate how lattice and subarray choices help maintain beam orthogonality even when the number of active elements is significantly lower than the FFT grid size. Through simulations, we show an SIR improvement of up to 20 dB compared to a baseline 16-point FFT configuration with 100 rectangularly placed elements and no tapering.

This paper is organized as follows: Section II introduces the mathematical formulation of the FFT for different coordinate systems. Section III presents the power pattern computation method, including unit cell modeling, subarray power pattern calculation, and array-level multibeam synthesis. Section IV analyzes multibeam scenarios comparing $N = M$ and $N < M$, evaluating power, interference, and SIR. Section V introduces strategies to maximize SIR, including array geometries, windowing, beam deactivation, and tapering. Evaluation Results and Discussion where we analyze the final results is presented in Section VI. Finally, Section VII concludes with key findings.

TABLE 2: System Parameters for the Evaluated MEO Satellite Communication Scenario.

Parameter	Value / Description
Satellite Orbit	Medium Earth Orbit (MEO)
Altitude	8000 km
Antenna Array	Planar phased array
Array Lattice Type	Rectangular or triangular
Antenna Elements	$N \times N$ elements
Beamforming Technique	2D FFT-based digital beamforming
Number of Beams	M^2 beams
Beamforming Location	On-board digital implementation
RF Chain Constraint	Fewer RF chains than antenna elements
Sub-array Strategy	Hexagonal or rectangular sub-array groupings
Polarization	Circular
Ground Terminal Sync	Perfect synchronization assumed

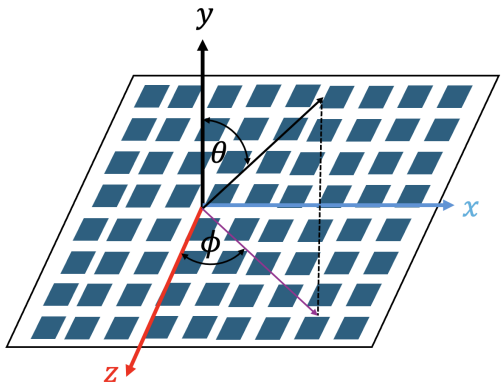

FIGURE 1: Coordinate system used for the mathematical formulation, detailing the x, y, and z axes.

II. SYSTEM MODEL, NOTATION, AND MATHEMATICAL FORMULATION

A. System Model

In this manuscript, we consider a multibeam satellite communication system operating in the Medium Earth Orbit (MEO) regime. The satellite is equipped with a planar phased array composed of N antenna elements per dimension, arranged either in a rectangular or triangular lattice, depending on the evaluated scenario. Beamforming is implemented digitally using a 2DFFT applied to the array outputs, enabling simultaneous generation of M^2 beams directed toward different user terminals within the satellite coverage footprint. The digital beamforming architecture assumes on-board implementation with constrained computational and power resources [17]. The number of RF chains is significantly lower than the total number of antenna elements, motivating the use of sub-array groupings. We focus on downlink communications, assuming perfect synchronization between satellite and ground terminals. Table 2 contains all the parameters of the system model presented in this study.

B. Notation

Table 3 summarizes the main symbols used throughout the paper.

C. FFT Mathematical Formulation

To accurately compute the beam power pattern using the FFT beamforming technique, it is essential to establish a reference coordinate system. The coordinate system used in this analysis is illustrated in Figure 1.

Let $\overrightarrow{x} = (1,0,0)$, $\overrightarrow{y} = (0,1,0)$, and $\overrightarrow{z} = (0,0,1)$ be the canonical unit vectors along the $x-$, $y-$, and $z-$axes, respectively. Then, the unit vector $\overrightarrow{r}_n$ in the direction of wave propagation (θ_n, ϕ_n) can be described as in (1):

$$\overrightarrow{r}_n = \sin\theta_n \cos\phi_n \overrightarrow{x} + \sin\theta_n \sin\phi_n \overrightarrow{y} + \cos\theta_n \overrightarrow{z}. \quad (1)$$

Additionally, employing the canonical unit-vector system, the position of every antenna element can be given in (2):

$$\tilde{p}_{[n_x,n_y,n_z]} = n_x d_x \overrightarrow{x} + n_y d_y \overrightarrow{y} + n_z d_z \overrightarrow{z}. \quad (2)$$

where d_x, d_y, d_z are the spacing gaps between antenna elements along the $x-$, $y-$, and $z-$axes, respectively; and

TABLE 3: Summary of Notations

Symbol	Description
N	Number of Antenna Elements per dimension
M	Index of the FFT
Y	Frequency Spectrum
AF	Array Factor
X	Symbols to Transmit
o, q	Indexes of the Beams
p_x, p_y	Period in the x-, y-Direction
W	Weight Matrices
k	Wave-Number
Z	Two-Dimensional DFT
$\overrightarrow{x}$, $\overrightarrow{y}$, $\overrightarrow{z}$	canonical unit vectors
θ_m, ϕ_m	Direction of Wave Propagation
$\overrightarrow{r}_n$	Wave Propagation Direction Unit Vector
E_o	Amplitude Scaling Factor
J_1	Bessel Function
r	Waveguide Aperture
$\hat{\theta}, \hat{\phi}$	Polar Unit Vectors
ϵ_r	Effective Permittivity
R	Power Pattern
h	High of the Satellite
R_e	Radius of the Earth
N_{Sub}	Number of elements in the sub-array
λ_0	Operational Wavelength
A	Amplitude Tapering
F_{array}	Far-Field Radiation Pattern
I	Interference
u, v	vector points in the uv plane
H	Phase response of the transformed array
θ_{-3dB}	Half-Power Beamwidth

n_x, n_y, n_z represent the position of antenna element on the array such as n_x-th column, n_y-th row, and n_z-th layer. Focusing on planar array settings, one can neglect the z-component. Then, the position formula given in (2) can be simplified for the planar-array antenna, as presented in (3):

$$\hat{p}_{[n_x,n_y]} = \tilde{p}_{[n_x,n_y,0]} = n_x d_x \overrightarrow{x} + n_y d_y \overrightarrow{y}. \tag{3}$$

Then, the beam propagation factor targeting the direction $\overrightarrow{r}_q$ from (n_x, n_y) element can be computed using (4):

$$a_{[n_x,n_y]}(\overrightarrow{r}_q) \approx e^{j\beta \hat{p}^T_{[n_x,n_y]} \overrightarrow{r}_q}, \tag{4}$$

where $\beta = -2\pi/\lambda$ and λ is the wave length.

This setup enables the derivation of expressions for calculating the final frequency spectrum, presented in (5):

$$Y_{[o,q]}(t) = \sum_{m_x=0}^{M_x} \sum_{m_y=0}^{M_y} X_{[m_x,m_y,o,q]}(t) e^{-i2\pi\left(\frac{m_x o p_x}{M_x} + \frac{m_y q p_y}{M_y}\right)}, \tag{5}$$

where X represents the transmitted symbols, and o, q are the indices of the desired beam, and p_x and p_y represents the period in wavelengths. This configuration implements the well-known FFT.

The radiation pattern is subsequently computed using the Aray Factor (AF) , presented in (6):

$$\text{AF} = \sum_{n_x=1}^{N_x} \sum_{n_y=1}^{N_y} |A_{n_x,n_y}| W_{[n_x,n_y,o,q]} e^{j(n_x)(\beta d_x \sin(\theta)\cos(\phi))} e^{j(n_y)(\beta d_y \sin(\theta)\sin(\phi))}, \tag{6}$$

where A_{m_x,n_y} denotes the amplitude weight matrix for each antenna element, β is the wave-number, and $W_{[m_x,n_y,o,q]}$ is the FFT beamforming matrix defined in (7):

$$W_{[m_x,m_y,o,q]} = Z X_{[m_x,m_y,o,q]} Z^T, \tag{7}$$

with Z being the Two-Dimensional Discrete Fourier Transform (2DDFT) matrix of M-points that includes the required progressive phase shifts, and $X_{[m_x,m_y,o,q]}$ specifies the active beam location.

In the FFT, the Fourier matrix Z_N, which plays a central role in efficiently performing the DFT, can be broken down into a series of simpler matrix operations. This breakdown involves iteratively applying a block diagonal butterfly matrix B, interspersed with permutation matrices and twiddle factor matrices, tailored to the structure of a radix-R FFT algorithm [18].

III. RADIATED POWER PATTERN COMPUTATION

The beamforming process utilizing the FFT is organized into four distinct and well-defined steps. Initially, the process begins with the computation of the power pattern for the unit cell. This is followed by the calculation of the subarray's power pattern, which is subsequently combined with the array factor of the entire array to enhance directivity and control beam shaping. In the next step, this combined pattern is integrated with the weight matrices derived from the M-point FFT, incorporating appropriate amplitude tapering to optimize beam performance and reduce SLL. The culmination of these steps results in a comprehensive grid distribution of beam patterns, systematically producing an M×M grid of beams in the operational bandwidth. This process is visually represented in Figure 2, providing a clear and graphical representation of each step involved. Detailed explanations of these steps are provided in the following subsections.

A. Unit Cell Power Pattern

For this analysis, we have selected a dielectric filled open-ended waveguide as radiating unit cell element. In this manuscript, the term of unit cell will refer to a single radiating element within the array. The radiation pattern of the open-ended waveguide is modeled by (8) for the total electric field $\mathbf{E}(r, \theta, \phi)$ emitted by a Right Hand Circularly Polarized (RHCP) wave [19]:

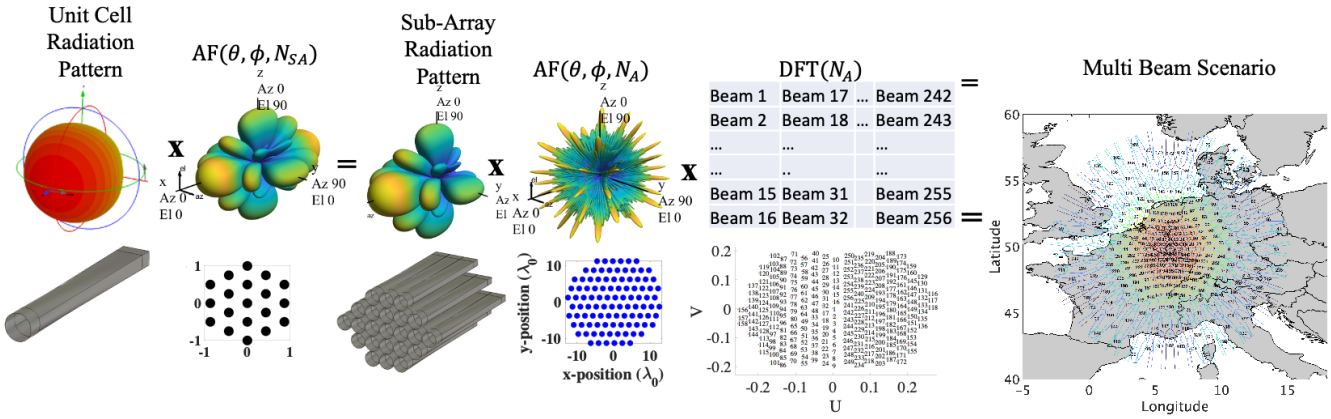

FIGURE 2: Simulation scenario as a step-by-step process.

$$\hat{\mathbf{E}}(r,\theta,\phi) = E_0 \frac{J_1\left(k_d a \sin\theta\right)}{ka\sin\theta} \frac{e^{-jkr}}{r} \left(\cos(\phi)\hat{\theta} + j\sin(\phi)\hat{\phi}\right) \tag{8}$$

where:

- E_0 is the amplitude scaling factor.
- J_1 represents the Bessel function of the first kind of order 1.
- $k_d = \frac{2\pi}{\lambda_0\sqrt{\epsilon_r}}$ is the wave number.
- ϵ_r denotes the effective permittivity inside the waveguide.
- a denotes the radius of the waveguide.
- r indicates the distance from the waveguide's aperture.
- θ and ϕ are the polar and azimuthal angles, respectively.
- $\hat{\theta}$ and $\hat{\phi}$ are unit vectors in the polar and azimuthal directions.

For ease of computation and understanding of results, we compute the normalized power pattern defined in (9).

$$\mathbf{R}(\theta,\phi) = \frac{|E(\theta,\phi)|^2}{\max\limits_{\theta,\phi}\left(|E(\theta,\phi)|^2\right)} \tag{9}$$

Assuming a future inter-element separation $p = 0.5\lambda_0$, we set the aperture of the waveguide to $a = 0.45\lambda_0$.

B. Subarray Power Pattern

The subarray component, defined as a cluster of unit cells connected to a single RF chain or beamformer, is arranged in a predefined lattice. This design reduces the number of RF-chains by gathering antennas that will share a common output. This reduces overall costs and complexity, which is quite convenient in a satellite scenario. The power pattern of each subarray is computed using the array factor formula, which integrates the contributions of individual elements within the subarray.

In addition,this analysis is intended to be used in a satellite scenario, we see convenient the use of subarrays. To determine the size of the subarray, we need to obtain the Field of View (FoV). For this, we assume that we are working in a MEO scenario where the satellite is orbiting in at $h = 8000$ km, over the earth surface. Then the FoV is calculated as (10)

$$\text{FoV} = \tan^{-1}\frac{R_e}{R_e + h}. \tag{10}$$

Assuming an Re= 6371 km, we obtain a FoV = 11.48°. Now, using (11) we can obtain that the inter-element separation that avoids any grating lobe in the FoV is p =2.5λ_0

$$p = \frac{\lambda_0}{2\sin\left(FoV\right)}. \tag{11}$$

The subarray configurations explored in this study include three distinct lattice arrangements. For all configurations, the period of the subarray is consistently set to $p_{sub} = 0.5\lambda_0$. The first configuration employs a rectangular lattice with 25 antenna elements, depicted in Figure 3.

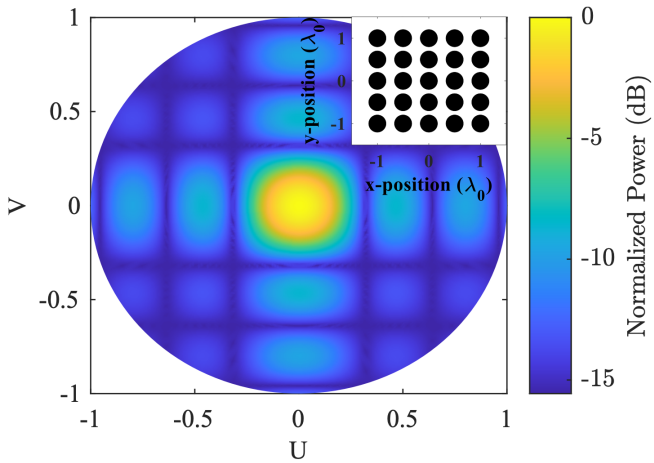

FIGURE 3: Power pattern of a subarray consisting of 5×5 antenna elements arranged in a square lattice with an inter-element spacing of 0.5λ_0.

The second configuration utilizes a triangular lattice with the same number of elements, where the element positions are transformed from the square lattice layout, as shown in Figure 4.

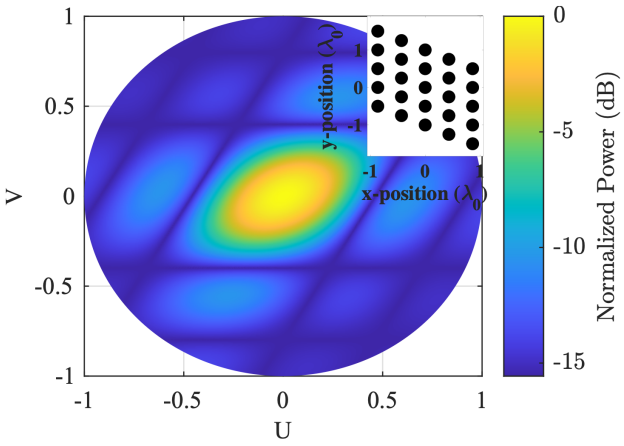

FIGURE 4: Power pattern of a subarray of 5x5 antenna elements distributed in a triangular lattice using an inter-element space of $0.5\lambda_0$.

Lastly, the third configuration is a modified triangular lattice, designed to form a hexagonal aperture. This design reduces the total number of elements to 19 to maintain symmetry, as illustrated in Figure 5.

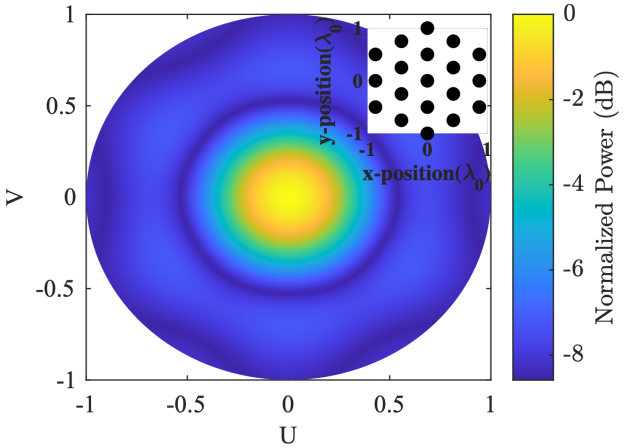

FIGURE 5: Power pattern of a subarray of 19 antenna elements distributed in a triangular lattice bounded by a hexagonal aperture, using an inter-element space of $0.5\lambda_0$.

Just to mention, this subarray configuration can be adapted to different antenna elements that follow (12).

$$N_{\text{Sub}} = 1 + 3n(n+1) \tag{12}$$

where:

- N_{Sub} is the total number of elements.
- n is the number of concentric hexagonal rings around the central element.

The realization of the subarrays within the overall array is illustrated in Figure 6a for n = 1 and Figure 6b for n = 2.

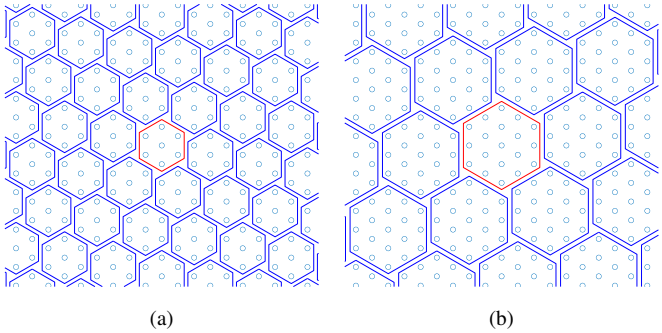

FIGURE 6: Comparison of hexagonal arrays with different numbers of elements. a) Hexagonal array with $N_{\text{Sub}} = 7$ elements. b) Hexagonal array with $N_{\text{Sub}} = 19$ elements.

It is noteworthy that this study assumes that the mutual coupling between antenna elements is below -20 dB, and therefore considered negligible. In addition, we also consider that the Active Element Pattern (AEP) and Active Element Impedance (AEI) are good enough to assume perfect operation in the whole frequency band. For future implementations, however, these parameters must be carefully evaluated to avoid blind spots during beam scanning and distortions in the final array pattern. For clarity, we define blind spots as regions where the effective coverage significantly diminishes due to insufficient overlap/ coverage of the Half-Power Beamwidth (HPBW) of adjacent radiation patterns.

C. Array

To generate the required beam power pattern for an M-point FFT, Algorithm 1 is employed. This algorithm extends its predecessor by incorporating the amplitude and phase contributions of the antenna elements.

The core computation begins with the algorithm iterating over each FFT steering position. At each position, it calculates the contribution from each antenna element by combining its individual radiation pattern with corresponding amplitude coefficients and phase shifts. These individual contributions are then summed to form the field pattern at each steering angle.

Following this, the computed field patterns are summed to derive the total power pattern for each steering position. The algorithm concludes by combining these power patterns with the subarray's inherent power pattern to produce the comprehensive power pattern across all steering directions.

Algorithm 1 Generate radiation pattern in multibeam scenario of an array using N_{array} antenna elements

Require: N_{array} ▷ Number of antenna elements in the array
Require: M ▷ Size of the 2DDFT
Require: $F_{\text{sub}}(\theta, \phi)$ ▷ Sub-array far-field pattern
Require: $\mathbf{P}_{\text{array}} = \{(x_1, y_1), (x_2, y_2), \ldots, (x_{N_{\text{array}}}, y_{N_{\text{array}}})\}$ ▷ Coordinates of antenna elements in the array
Require: $A(m, n)$ ▷ Amplitude excitation
Require: W = 2DDFT(M) ▷ Phase shift matrix using 2DDFT
Require: λ ▷ Wavelength of the signal
Require: θ, ϕ ▷ Observation angles (range)
Ensure: $F_{\text{array}}(\theta, \phi)$ ▷ Far-field radiation pattern
$k \leftarrow \frac{2\pi}{\lambda}$ ▷ Calculate wave number
for $m \leftarrow 1$ to M^2 **do**
  $F_{\text{array}}(\theta, \phi, m) \leftarrow 0$ ▷ Initialize total field per beam
  for all (θ, ϕ) in observation angles **do**
    for $n \leftarrow 1$ to N^2 **do**
      $\psi_n(\theta, \phi) \leftarrow k(x_n \cos\theta \cos\phi + y_n \cos\theta \sin\phi)$
      $I_{n,m} = A_{n,m} W n, m$
      $D_{n,m}(\theta, \phi) \leftarrow I_{n,m} e^{j\psi_n(\theta,\phi)}$
      $F_{\text{array}}(\theta, \phi, m) \leftarrow F_{\text{array}}(\theta, \phi, m) + D_{n,m}(\theta, \phi)$
    end for
  end for
$F_{\text{array}}(\theta, \phi, m) \leftarrow F_{\text{sub}} F_{\text{array}}(\theta, \phi, m)$
end for
Output $F_{\text{array}}(\theta, \phi, m)$

IV. MULTIBEAM GENERATION

A. Case A: $N = M$

1) Beam Pattern

As a preliminary approach, we utilize a 16-point FFT ($M = 16$), deploying 256 antennas arranged in a square lattice ($N = 16$) elements per dimension. Each subarray within the array consists of $N_{\text{sub}} = 5$ elements, also configured as a square lattice. Figure 7 illustrates this setup, depicting the half-power beamwidth θ_{-3dB} of the power pattern for all 256 beams.

Analysis of Figure 7 indicates that the beams are systematically organized into a regular square lattice, exhibiting varying power levels across the grid. This variation is visually delineated through a color gradient; centrally located beams are significantly more powerful than those near the edges. Such attenuation in power stems from the subarray's power pattern, which effectively serves as a masking element that modulates the output power of all generated beams.

Furthermore, the θ_{-3dB} of all beams do not overlap, indicating a potential for high Signal-to-Interference Ratios (SIR). The grating lobes are particularly noticeable in regions where beams are produced at the peripheral. Those beams can be configured so that they can radiate outside the FoV.

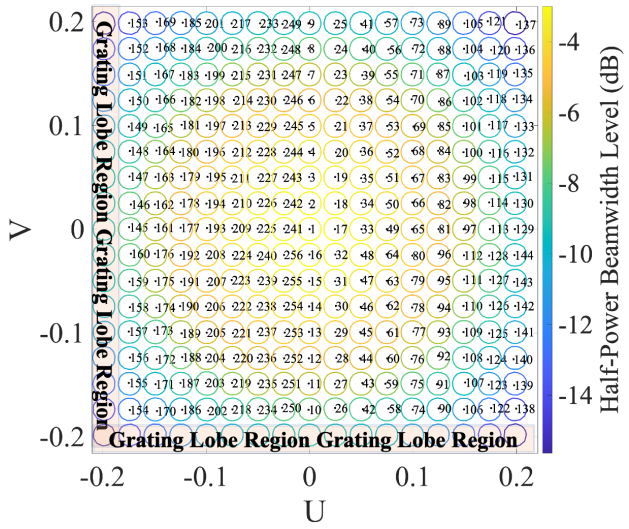

FIGURE 7: θ_{-3dB} power pattern for the scenario $N = M$, which uses a 16-point FFT and ($N = 16$) antennas per dimension arranged in a square lattice. Each array consists of subarrays with $N_{\text{sub}} = 5$ elements per dimension, also arranged in a square lattice.

Examining the central beam pattern (beam pattern #1), depicted in Figure 8, shows that the beams have a maximum SLL of approximately 13 dB, characteristic of a square aperture.

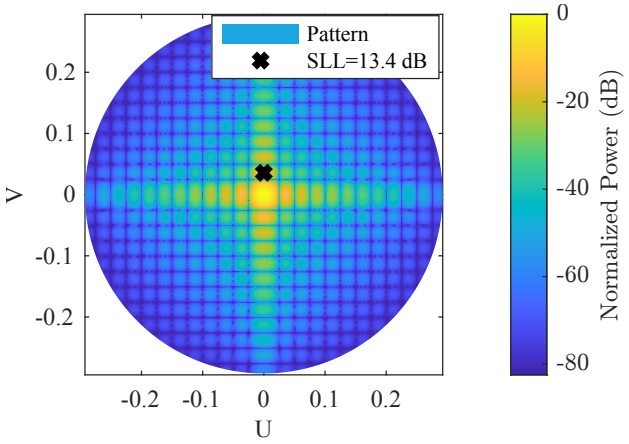

FIGURE 8: Power pattern corresponding to the central beam using an FFT of a rectangular array of 16×16 elements with a subarray configuration of 5×5 antenna elements.

2) Signal-to-Interference Ratio

The overall SIR in this multibeam scenario can be computed using (13).

$$SIR = \frac{R_{\text{maximum}}}{I} \tag{13}$$

where R_{maximum} is the total maximum radiated power per beam and I is the interference.

The SIR, illustrated in Figure 9, reveals several interesting insights. First, high peaks in the SIR are observed at the center of the beam, which can be attributed to the orthogonality of the FFT when $N = M$. This orthogonality ensures that, at the maximum of each beam, the interference from other beams is minimal due to their nulls. Additionally, as we move away from the beam center, the SIR decreases, which is caused by the reduction in beam power and the increasing interference from adjacent beams.

It should also be noted that the maximum SIR values reach around 60 dB, which easily supports the establishment of reliable high-throughput communication.

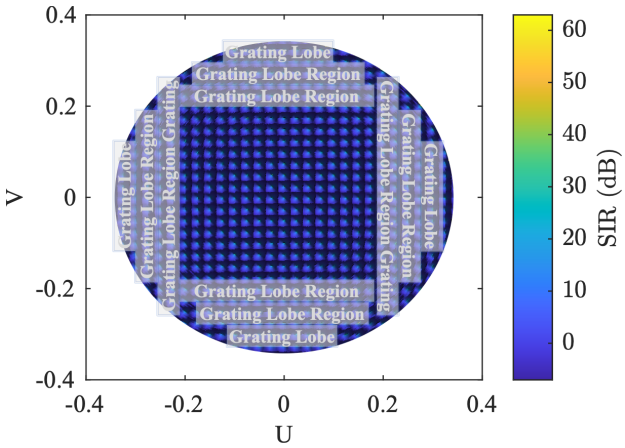

FIGURE 9: SIR calculated using an FFT of a 16×16 rectangular array with 5×5 rectangular subarrays of antenna elements.

B. Case A: $N < M$

The previously presented beam distribution reveals the existence of blind spot regions between beams, where prospective users would experience service outages. To mitigate this issue while simultaneously reducing the number of RF-chains, we have selected the case of $N = 10$ with a 16-point FFT, which results in broader beams that effectively eliminate blind spots. In this configuration, Algorithm 1 remains applicable, albeit with minor modifications. Specifically, the 2DDFT matrix is windowed to an $N \times N$ dimension.

Figures 10 and 11 represent the beam distribution at the $\theta_{-3\text{dB}}$ points for this configuration, together with the corresponding SIR.

Analyzing the results, we can infer that reducing the number of antennas from 256 to 100 introduces the following changes:

- The $\theta_{-3\text{dB}}$ of all beams has widened due to the reduction in the overall size of the antenna array, which is proportional to the decrease in directivity. This expansion helps reduce the blind spots mentioned in the previous section.
- The generated beams are no longer orthogonal, resulting in increased overall interference.
- The SIR is drastically reduced, with a maximum value of -1.93 dB, which significantly limits the ability to support high-throughput communications.

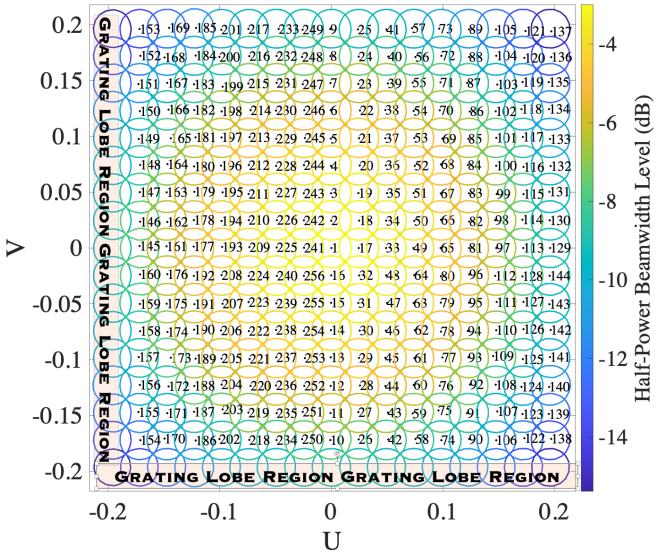

FIGURE 10: $\theta_{-3\text{dB}}$ power pattern for the scenario $N < M$, which uses a 16-point FFT using $N = 10$ antennas per dimension arranged in a square lattice. Each array consists of subarrays with $N_{\text{sub}} = 5$ elements per dimension, also arranged in a square lattice.

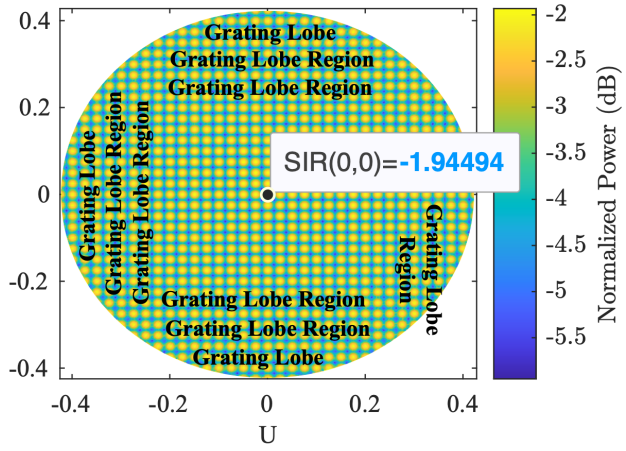

FIGURE 11: SIR for the first beam index, using an FFT of a 10×10 array of elements, with rectangular subarrays of 5×5 antenna elements.

V. TECHNIQUES TO MAXIMIZE SIR

To maximize the SIR, we analyze three main scenarios. The first scenario involves studying different antenna lat-

tices compatible with the FFT beamforming algorithm. The second scenario explores the application of windowing techniques to improve the SLL. The third scenario investigates the 4-color scheme application. Finally, we combine all the techniques including amplitude tapering. In the following sections, we detail the first two scenarios.

A. Array and Subarray Lattices

The FFT beamforming algorithm, in its basic form, is compatible with rectangular regular arrays, but the use of a triangular lattice is also valid. The array positions for the rectangular regular array, defined in (2) can be separated into X_0 and Y_0 scalar positions, as presented by (14):

$$\begin{aligned} x_0 &= m d_x \lambda_0, \quad \forall m \in \{0, \ldots, M_x - 1\}, \\ y_0 &= n d_y \lambda_0, \quad \forall n \in \{0, \ldots, M_y - 1\}, \end{aligned} \tag{14}$$

To transform the rectangular positions into a triangular lattice, we use the matrix transformation shown in (15):

$$\begin{bmatrix} x \\ y \end{bmatrix} = \begin{bmatrix} \frac{\sqrt{3}}{2} & 0 \\ -\frac{1}{2} & 1 \end{bmatrix} \begin{bmatrix} x_0 \\ y_0 \end{bmatrix} \tag{15}$$

The transformed positions of the array are then determined by (16):

$$\begin{aligned} x &= m \frac{\sqrt{3}}{2} d_x \lambda_0, \\ y &= -\frac{1}{2} m d_x \lambda_0 + n d_y \lambda_0, \end{aligned} \tag{16}$$

Now, with the positions, we can analyze the phase response of the transformed array by (17) and becomes (18):

$$H = \exp\left(j \frac{2\pi}{\lambda} (ux + vy)\right) \tag{17}$$

where u and v are vector points to be determined in the uv-plane. Applying the transformation, we obtain (18):

$$H = \exp\left[j \frac{2\pi}{\lambda} \left(um \frac{\sqrt{3}}{2} d_x \lambda_0 + v \left(-\frac{1}{2} m d_x \lambda_0 + n d_y \lambda_0\right)\right)\right] \tag{18}$$

Next, consider the phase response of the 2D FFT with array indices q and p, as given by (19):

$$W = \exp\left[j 2\pi \left(\frac{qm}{M_x} + \frac{pn}{M_y}\right)\right] \tag{19}$$

By equating the phase response of the 2D FFT in (19) with the phase response of the transformed array in (18), we obtain the positions of the generated beams in the uv plane:

$$\begin{aligned} v &= \frac{p}{\lambda_0 M_y d_y}, \\ u &= \frac{2}{\sqrt{3}} \left(\frac{q}{\lambda_0 M_x d_x} + \frac{p}{2\lambda_0 M_y d_y}\right), \end{aligned} \tag{20}$$

To maintain a uniform distribution of antenna elements, the transformation must be applied to both the array and subarray positions (as shown in Figure 4). Using this array and subarray lattice, we can improve beam distribution.

The beam distribution for an array of $N = 10$ antennas arranged in a triangular lattice using a 16-point FFT is illustrated in Figure 12.

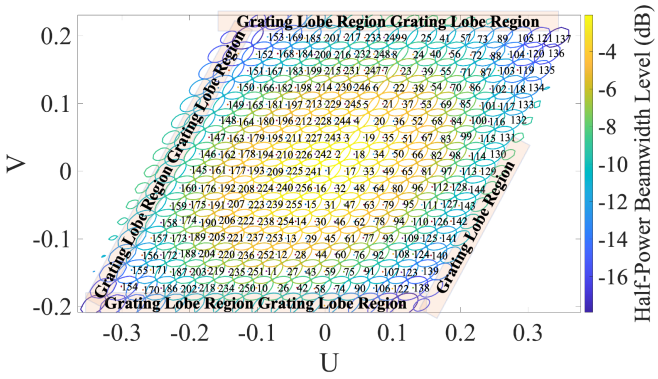

FIGURE 12: Power pattern at $\theta_{-3\text{dB}}$ using a 16-point FFT with $N = 10$ antennas per dimension arranged in a triangular lattice. Each array consists of subarrays with $N_{\text{sub}} = 5$ elements per dimension, also arranged in a triangular lattice.

In addition to the modified beam lattice, this beam distribution shows some differences compared to the rectangular lattice. The most noticeable change is that the generated beams no longer exhibit symmetrical beamwidths. This variation arises from the new antenna distribution, which follows a parallelepiped aperture rather than a square one. Moreover, the grating lobes are more numerous but exhibit reduced beamwidth, meaning that depending on the position, the grating lobe may have a wider or narrower beamwidth. This behavior is primarily influenced by the subarray beam pattern.

The SIR of this configuration, illustrated in Figure 13, shows that the SIR has not improved but has slightly decreased. Although this configuration does not enhance the SIR, it reduces blind spots compared to the square configuration.

B. Windowing

One of the main drawbacks of using a triangular lattice aperture is the asymmetry in the beamwidths of the generated beams. As mentioned above, this asymmetry arises due to the shape of the array. To overcome this limitation, spatial windowing can be applied to the full array. To obtain an aperture with a specific number of elements and symmetrical beamwidths, we can select the antenna elements starting from the center of the array and moving outward in a radial manner until we reach the desired number of antennas. This type of windowing allows us to obtain a quasi-symmetric beam aperture. This concept is visually depicted in Figure 14.

To analyze the advantages of this configuration, we examine the beam pattern distribution and SIR with a total of

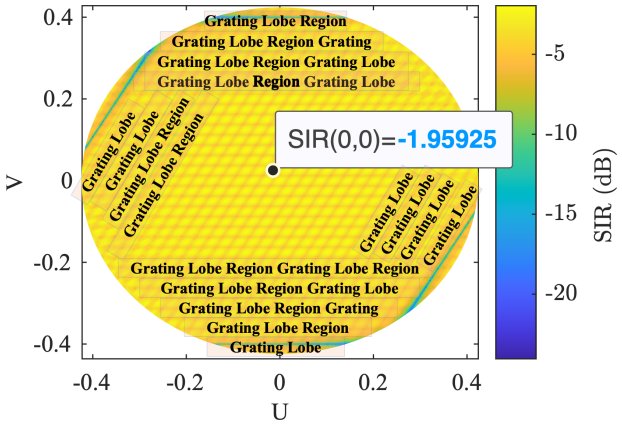

FIGURE 13: SIR for the first beam index using an FFT of a triangular array of $N = 10$ elements with triangular subarrays of 5×5 antenna elements.

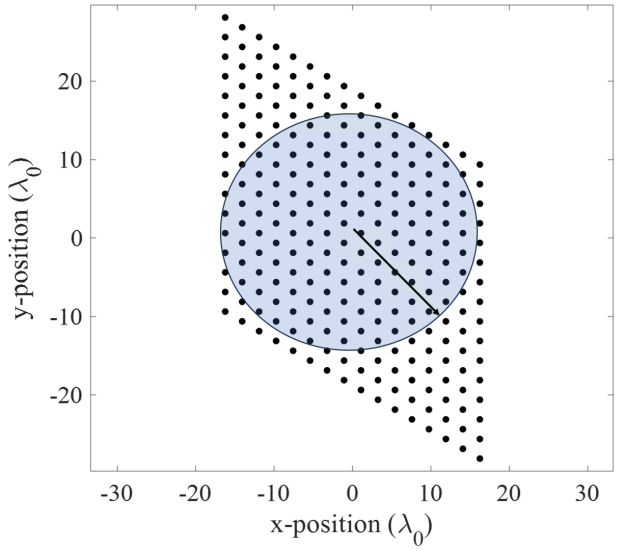

FIGURE 14: Circular windowing approach applied to an array with a triangular lattice.

100 antenna elements, where each subarray has 19 elements distributed in a hexagonal lattice. The beam distribution for this configuration is shown in Figure 15.

In this case, the beam distribution follows the envelope of the subarray power pattern, which is a notable difference from the previous configuration. Moreover, the beamwidths are symmetric because of the circular aperture. However, the computed SIR, illustrated in Figure 16, does not show any improvement compared to previous scenario; therefore we need to use other techniques that allows to reduce interference.

C. Beam Deactivation

Given that the previous scenarios do not achieve the desired improvement in SIR, we propose using the 4-color scheme.

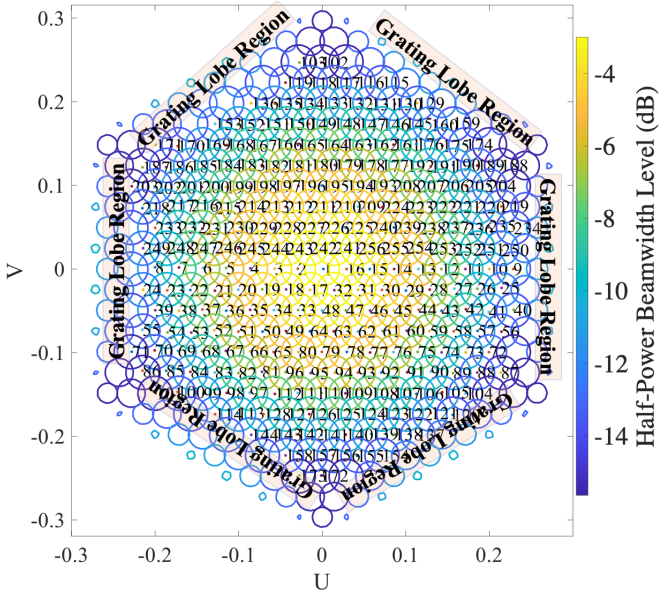

FIGURE 15: Power pattern at $\theta_{-3\text{dB}}$ using a 16-point FFT with $N_{\textbf{total}} = 100$ antennas distributed in a triangular lattice with a circular aperture. Each array is composed of subarrays with $N_{\textbf{sub}_{\textbf{total}}} = 19$ elements, arranged in a hexagonal aperture.

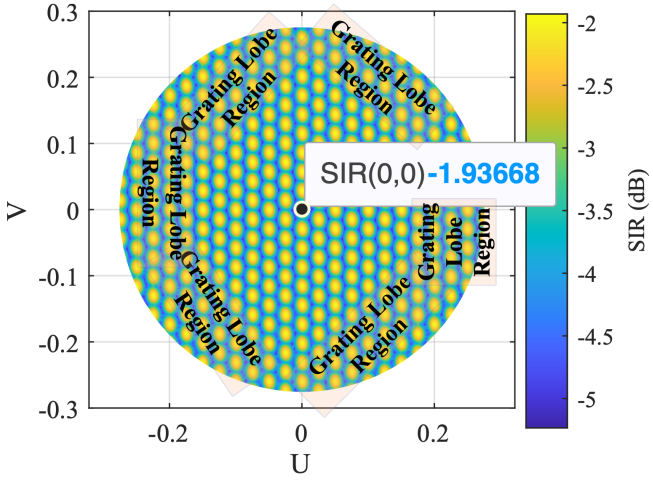

FIGURE 16: SIR corresponding to an FFT of a hexagonal aperture array of 91 elements, using a hexagonal subarray of 19 antenna elements.

Although the 4-color frequency reuse scheme is simple and robust, it is inherently less spectrally efficient because not all beams operate on the same frequency or polarization simultaneously. This limitation restricts the maximum number of simultaneously active beams, particularly when using conservative spatial frequency reuse patterns, which can reduce overall throughput. However, integrating this scheme with FFT-based digital beamforming techniques offers the opportunity to blend reliability with performance gains. This

approach allows us to utilize all 256 beams, but in groups of four, differentiated by polarization and frequency. In this scheme, we select 64 out of the 256 beams at a time to evaluate the SIR. The concept is visually depicted in Figure 17, and the resulting SIR for the first scenario is shown in Figure 18.

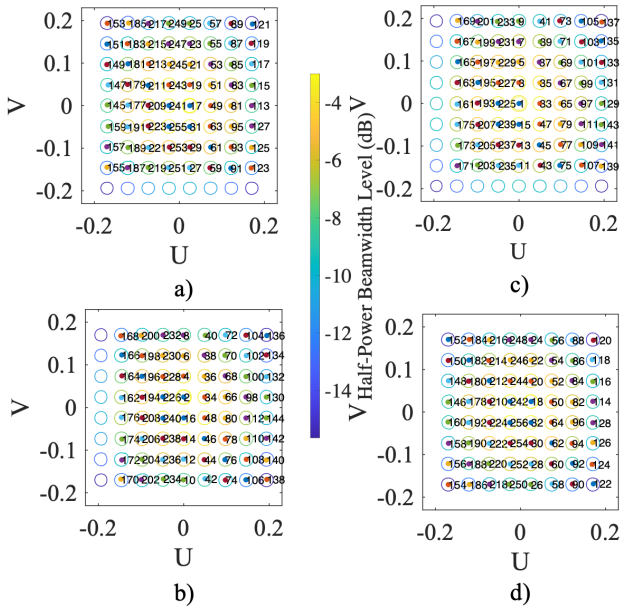

FIGURE 17: Power pattern at $\theta_{-3\text{dB}}$ using a 16-point FFT with $N_{\textbf{total}} = 100$ antennas distributed in a rectangular lattice. (a) Represents the first set of 64 beams transmitting with polarization P_1 and frequency f_1. (b) Represents the second set of 64 beams transmitting with polarization P_2 and frequency f_1. (c) Represents the third set of 64 beams transmitting with polarization P_2 and frequency f_2. (d) Represents the fourth set of 64 beams transmitting with polarization P_1 and frequency f_2.

The calculated results show that, under these conditions, communication is feasible, as the SIR reaches a maximum of 7.43 dB across the four scenarios. However, one drawback of this configuration is that the beam lattice does not offer the improved coverage that a triangular lattice provides. Therefore, the next subsection will address the combination of the studied techniques and the incorporation of amplitude tapering.

D. Combination of triangular lattice, beam deactivation and windowing

An interesting aspect of the beam deactivation scenario, is that since the main beams are spaced farther apart, the interference primarily arises from the SLL of each beam, which interferes with the main beams. Therefore, to improve the SIR, we need to reduce the SLL. Additionally, since deactivating some beams creates space between them, there is room to widen the remaining beams. One effective method for reducing the SLL is applying tapering to the

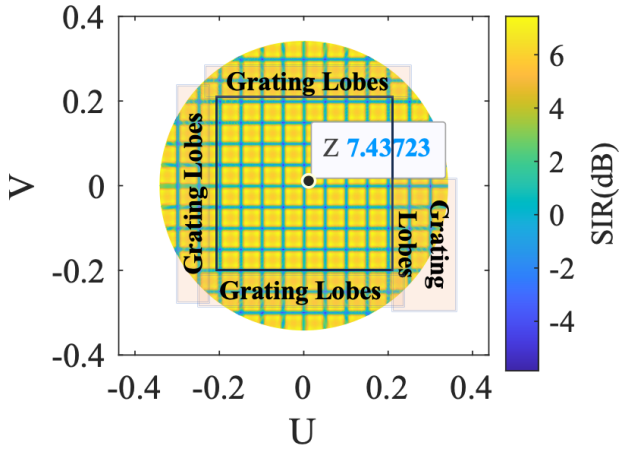

FIGURE 18: SIR using a 16-point FFT with $N_{\textbf{total}} = 100$ antennas distributed in a rectangular lattice for the first set of 64 beams with polarization P_1 and frequency f_1.

antenna elements. There are two common types of tapering: windowing and amplitude tapering. In this section, we will combine the techniques of beam deactivation, windowing, and amplitude tapering.

In the first scenario, we use a circular aperture with $N_{\textbf{total}} = 100$ subarray antenna elements. The elements in each subarray are arranged to form a hexagonal aperture with $N_{\text{sub}} = 19$. The beam distribution for one of the colors is shown in Figure 19. From the results, we can observe that the array's aperture generates nearly symmetric beams, which allow for better tessellation.

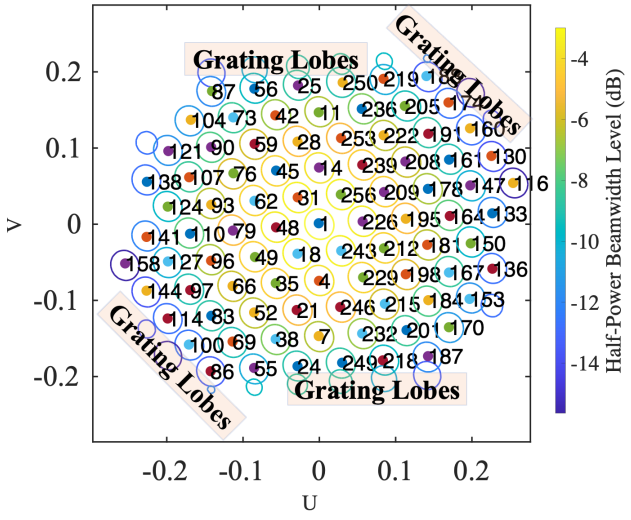

FIGURE 19: Power pattern at $\theta_{-3\text{dB}}$ for one of the four color schemes. The array uses a 16-point FFT with $N_{\textbf{total}} = 100$ antennas distributed in a hexagonal lattice using hexagonal aperture subarrays.

Now, analyzing the SIR, illustrated in Figure 20, we can see that the maximum value reaches 8.35 dB. This

represents an improvement of 1 dB compared to the previous scenario. This increase is due to the contribution of the circular aperture and the triangular lattice, which reduces interference.

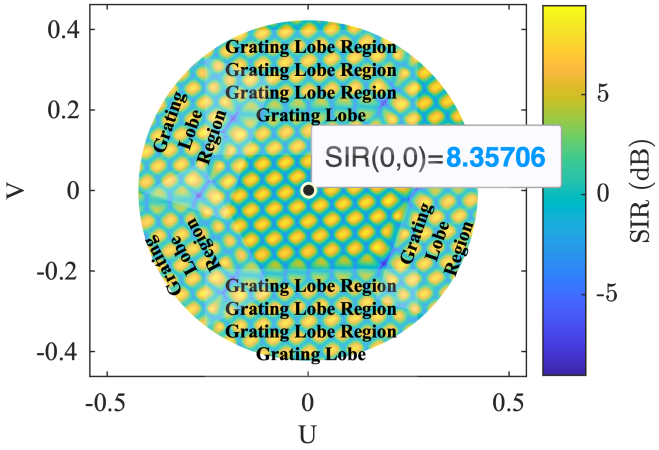

FIGURE 20: SIR for the beam distribution shown in Figure 19.

E. Integration of triangular lattice, beam deactivation, circular aperture, and tapering techniques

In this configuration, we explore the combined application of beam deactivation, circular aperture, and antenna element tapering to enhance system performance. Although tapering is not the most power efficient method due to increased heat dissipation, elements not working to their full capacity, or elements tailored to certain power requirements, it is crucial to evaluate its potential for improving the SIR through controlled amplitude tapering.

For this purpose, the Chebyshev tapering technique is employed to reduce sidelobe levels while preserving the narrow beamwidth of the main lobe. This method uses weighting coefficients derived from Chebyshev polynomials to achieve a specified sidelobe level with the minimum possible main lobe widening [19]. The resulting amplitude distribution provides a compromise between uniform and tapered excitation. The taper values derived from the Chebyshev window are assigned across the entire antenna array. Subsequently, elements with lower taper values are deactivated (windowed), preserving only those with higher taper values. This selective activation effectively combines tapering with beam deactivation, aiming to suppress sidelobes and enhance the SIR.

This methodology is visually represented in Figure 21, illustrating the tapering and deactivation process. The resulting beam pattern for the central beam is depicted in Figure 22, demonstrating the impact of the integrated approach on beam shaping and interference reduction.

To facilitate understanding, we computed the corresponding SIR for various tapering levels, as shown in Figure 23.

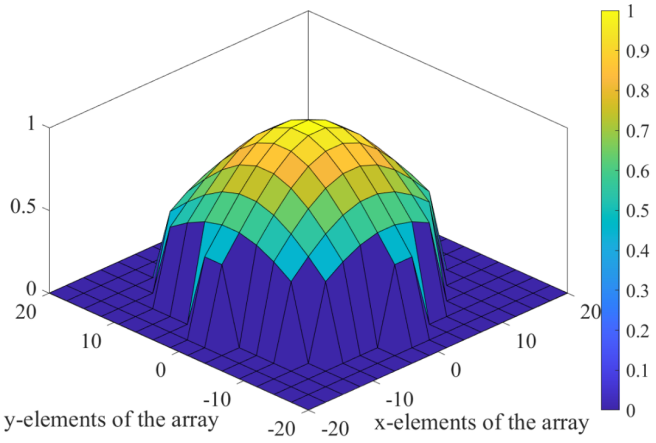

FIGURE 21: Tapering applied to the antenna elements, including the effect of windowing.

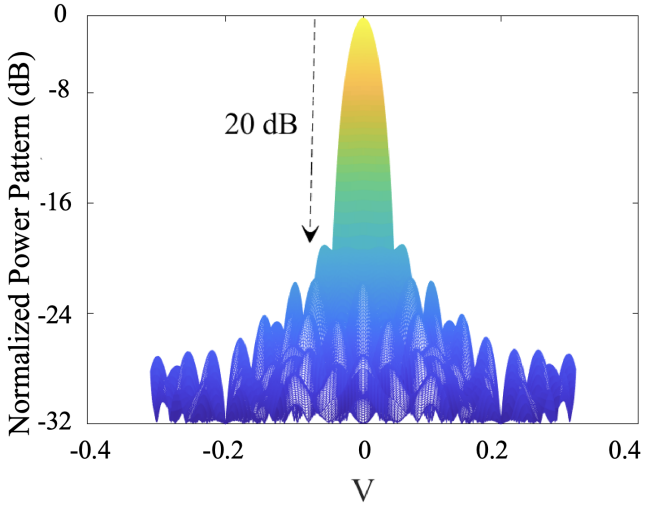

FIGURE 22: Tapered beam pattern corresponding to antenna using the tapering + windowing illustrated in Figure 21

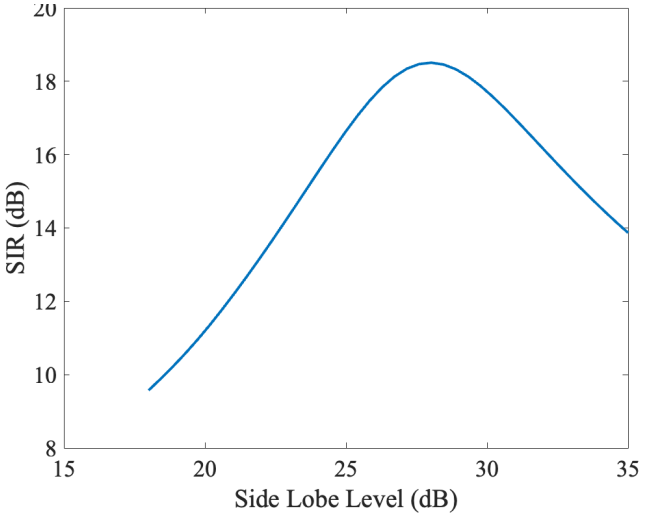

FIGURE 23: SIR vs. SLL for a triangular beam distribution.

VI. EVALUATION RESULTS AND DISCUSSION

The results obtained from the combination of all proposed techniques indicate that tapering significantly enhances the SIR, reaching a peak value of 18 dB when the tapering yields an SLL of 28 dB. In this case, a balance is achieved between low interference from both the SLL and the main beams. However, as the SLL increases beyond this point, the SIR begins to decline. This is because, although the interference from the sidelobes continues to decrease, the beamwidths become wider, eventually leading to overlap between adjacent beams, resembling the behavior observed in the baseline scenario. In practical implementations, several factors must be taken into account beyond the algorithmic design. The application of amplitude tapering requires a reliable and precise amplitude control system, which introduces additional hardware complexity and power consumption. Furthermore, ensuring accurate performance depends on proper calibration of both amplitude and phase across the array elements, which may be affected by manufacturing tolerances, temperature variations, and aging effects. These challenges are further amplified in the space environment, where radiation exposure and thermal cycling can impact the long-term reliability of the components.

Moreover, while tapering is the technique that contributes most significantly to improving the SIR, it is not effective in isolation. It requires beam deactivation to function optimally. Beam deactivation introduces additional degrees of freedom, allowing the system to increase beamwidths while reducing the SLL without incurring additional interference.

Finally, the use of a triangular beam placement grid helps to avoid coverage gaps, offering a more uniform coverage pattern compared to rectangular arrangements. The main findings discussed in this paper are summarized in Table 4.

TABLE 4: Comparison of Configurations

Configuration	Pros	Cons
Triangular Lattices	Better beam allocation, fewer blind spots.	Aperture becomes asymmetric with FFT.
Triangular Lattices + Windowing	Improves SLL, symmetric beams.	No overall SIR improvement.
Triangular Lattices + Windowing + Beam Deactivation	SIR gain $\approx$ 8 dB due to the reduced interference	Requires 4-color scheme to avoid blind spots.
All techniques	Increases SIR $\approx$ 18 dB by lowering sidelobe interference.	Needs amplitude control; higher cost and complexity.

To clearly highlight the research gaps in existing studies and to contextualize the novelty of our proposed approach, Table 5 provides a structured comparison of related works. The comparison focuses on key technical aspects including the beamforming technique, lattice type, use of subarrays, application of the 4-color scheme, implementation of amplitude tapering, and whether the work combines multiple techniques.

TABLE 5: Comparison of Related Works with the Proposed Approach

Ref.	BF Tech.	Lattice Type	Sub Arrays	4-Color	Taper	$N < M$	Complex. & Power Consump.
[5]	NUFFT	Irre.	✗	✗	✗	✗	High
[20]	FFT	Trian.	✗	✓	✗	✗	Low
[9]	FFT	Rect.	✗	✗	✗	✗	Low
CW	FFT	Trian.	✓	✓	✓	✓	Low

VII. CONCLUSION

In this paper, we explored the application of FFT-based digital beamforming for multibeam satellite communication systems, focusing on optimizing antenna lattice configurations and improving the SIR. For subarrays and arrays, we analyzed various antenna lattice structures, including rectangular, triangular, and hexagonal configurations, and examined the impact of reducing the number of antenna elements relative to the FFT size. Our findings highlight that while reducing the number of antenna elements can lead to decreased power consumption and system mass, it also results in a degraded SIR due to wider beamwidths and increased interference. To mitigate these effects, we explored beam deactivation, spatial windowing, and amplitude tapering, which have proven to be an effective approach to improve SIR in scenarios with reduced antenna elements, particularly in systems where space and power are limited. Our results indicate that applying an appropriate tapering method significantly improves the SIR, reaching a maximum of 18 dB when the SLL is reduced to 27 dB. While this work primarily focuses on maximizing SIR as the main performance metric, we acknowledge that other criteria—such as power efficiency, computational complexity, coverage uniformity, and beam switching speed—are also essential in practical satellite communication systems. These aspects will be addressed in future work through detailed system-level studies and hardware validations. These insights demonstrate the potential of FFT-based beamforming in enabling more efficient satellite communication systems, particularly in the context of large multibeam antenna arrays. Future research will focus on further optimization of array configurations and beamforming algorithms, including the application of additional techniques such as array thinning. Furthermore, hardware validation of the proposed approach is planned as part of ongoing and future work. Specifically, the method will be implemented on an FPGA (Virtex UltraScale+ VCU129) for the beamforming algorithm, including auxiliary modules, and on the RFSoC (Zynq UltraScale+ RFSoC ZCU111) for the RF front-end. The system will be tested using a built-in channel emulator to assess its

performance under realistic conditions, including hardware constraints and channel impairments.

REFERENCES

[1] R. Palisetty, G. Eappen, J. L. G. Rios, J. C. M. Duncan, S. Domouchtsidis, S. Chatzinotas, B. Ottersten, B. Cortazar, S. D'Addio, and P. Angeletti, "Area-power analysis of fft based digital beamforming for geo, meo, and leo scenarios," in *2022 IEEE 95th Vehicular Technology Conference: (VTC2022-Spring)*, pp. 1–5, 2022.

[2] K. Yang, Z. Zhao, J. Liu, and Q. H. Liu, "Robust adaptive beamforming using an iterative fft algorithm," *Signal Processing*, vol. 96, pp. 253–260, 2014.

[3] R. N. Bracewell, *The Fourier Transform and Its Applications*. McGraw-Hill, 2000.

[4] L. M. Garcés-Socarrás, J. L. González-Rios, R. Palisetty, R. Cuiman, V. N. Ha, J. A. Vásquez-Peralvo, G. Eappen, T. T. Nguyen, J. C. M. Duncan, S. Chatzinotas, B. Ottersten, C. L. Marcos, A. Coskun, S. King, S. D'Addio, and P. Angeletti, "Efficient digital beamforming for satellite payloads using a 2d fft-based parallel architecture," in *2025 IEEE International Symposium on Circuits and Systems (ISCAS)*, pp. 1–5, 2025.

[5] P. Angeletti, A. Coskun, and I. Kale, "Reconfigurable digital beamforming network," Jan. 4 2024. US Patent App. 18/346,586.

[6] I. n. A. Xilinx, *Fast Fourier Transform v9.1 LogiCORE IP Product Guide*, 2022. Configurable streaming FFT core supporting 8–14 bit quantization, up to 65536-point transforms.

[7] S. Haykin and K. R. Liu, *Handbook on array processing and sensor networks*. John Wiley & Sons, 2010.

[8] V. N. Ha, D. H. Nguyen, J. C.-M. Duncan, J. L. Gonzalez-Rios, J. A. V. Peralvo, G. Eappen, L. M. Garces-Socarras, R. Palisetty, S. Chatzinotas, and B. Ottersten, "User-centric beam selection and precoding design for coordinated multiple-satellite systems," in *2024 IEEE 35th International Symposium on Personal, Indoor and Mobile Radio Communications (PIMRC)*, pp. 1–6, IEEE, 2024.

[9] I. Chiba, R. Miura, T. Tanaka, and Y. Karasawa, "Digital beam forming (dbf) antenna system for mobile communications," *IEEE Aerospace and Electronic Systems Magazine*, vol. 12, no. 9, pp. 31–41, 1997.

[10] A. Madanayake, V. Ariyarathna, S. Madishetty, S. Pulipati, R. J. Cintra, D. Coelho, R. Oliviera, F. M. Bayer, L. Belostotski, S. Mandal, and T. S. Rappaport, "Towards a low-swap 1024-beam digital array: A 32-beam subsystem at 5.8 ghz," *IEEE Transactions on Antennas and Propagation*, vol. 68, no. 2, pp. 900–912, 2020.

[11] V. Ariyarathna, D. F. G. Coelho, S. Pulipati, R. J. Cintra, F. M. Bayer, V. S. Dimitrov, and A. Madanayake, "Multibeam digital array receiver using a 16-point multiplierless dft approximation," *IEEE Transactions on Antennas and Propagation*, vol. 67, no. 2, pp. 925–933, 2019.

[12] R. Palisetty, L. M. Garces Socarras, H. Chaker, V. Singh, G. Eappen, W. A. Martins, V. N. Ha, J. A. Vásquez-Peralvo, J. L. Gonzalez Rios, J. C. Merlano Duncan, S. Chatzinotas, B. Ottersten, A. Coskun, S. King, S. D'Addio, and P. Angeletti, "Fpga implementation of efficient beamformer for on-board processing in meo satellites," in *2023 IEEE 34th Annual International Symposium on Personal, Indoor and Mobile Radio Communications (PIMRC)*, pp. 1–7, 2023.

[13] P. Angeletti, "Multiple beams from planar arrays," *IEEE Transactions on Antennas and Propagation*, vol. 62, no. 4, pp. 1750–1761, 2014.

[14] J. O. Coleman, *Planar arrays on lattices and their FFT steering, a primer*. Naval Research Laboratory, 2011.

[15] A. Camps, J. Bará, I. C. Sanahuja, and F. Torres, "The processing of hexagonally sampled signals with standard rectangular techniques: Application to 2-d large aperture synthesis interferometric radiometers," *IEEE Transactions on Geoscience and Remote Sensing*, vol. 35, no. 1, pp. 183–190, 1997.

[16] W. P. M. N. Keizer, "Low sidelobe pattern synthesis of array antennas with a triangular or skew lattice using the ift method," *IEEE Open Journal of Antennas and Propagation*, vol. 4, pp. 1000–1015, 2023.

[17] Q. Ouyang, Z. Qu, and Y. Gao, "A novel distributed beamforming scheme based on phase adjustment and dynamic tracking for leo satellite communications," *IEEE Transactions on Vehicular Technology*, vol. 74, no. 6, pp. 9391–9403, 2025.

[18] J. A. Vásquez-Peralvo, J. C. Merlano Duncan, V. N. Ha, R. Palisetty, G. Eappen, L. M. Garcés-Socarrás, J. L. González Rios, P. H. Aldás Ponce, and S. Chatzinotas, "Quantization effects of twiddle factors in fft for beamforming using planar arrays," in *2024 IEEE International Symposium on Phased Array Systems and Technology (ARRAY)*, pp. 1–7, 2024.

[19] C. A. Balanis, *Antenna Theory: Analysis and Design*. Wiley, 4th ed., 2016.

[20] P. Angeletti and R. De Gaudenzi, "A pragmatic approach to massive mimo for broadband communication satellites," *IEEE Access*, vol. 8, pp. 132212–132236, 2020.